Electronic structure and magnetic properties of 3*d*-4*f* double perovskite material

S. Kundu,[1] A. Pal,[1] Amit Chauhan,[2,3,4] K. Patro,[1] K. Anand,[5] S. Rana,[6] V. G. Sathe,[6] Amish G. Joshi,[7] P. Pal,[8] K. Sethupathi,[1,9] B. R. K. Nanda,[2,3,4,*] and P. Khuntia[1,9,4,†]

[1]*Department of Physics, Indian Institute of Technology Madras, Chennai 600036, India*
[2]*Condensed Matter Theory and Computational Lab, Department of Physics, Indian Institute of Technology Madras, Chennai 600036, India*
[3]*Center for Atomistic Modelling and Materials Design, Indian Institute of Technology Madras, Chennai 600036, India*
[4]*Functional Oxide Research Group, Indian Institute of Technology Madras, Chennai 600036, India*
[5]*Department of Physics, Indian Institute of Technology (BHU), Varanasi 221005, India*
[6]*UGC-DAE Consortium for Scientific Research, University Campus, Khandwa Road, Indore 452001, India*
[7]*CSIR-Central Glass & Ceramic Research Institute, Naroda Centre, 168-169 Naroda Industrial Estate, Ahmedabad 382330, India*
[8]*CSIR-Central Glass & Ceramic Research Institute, 196 Raja S. C. Mullick Road, Kolkata 700032, India*
[9]*Quantum Centre for Diamond and Emergent Materials, Indian Institute of Technology Madras, Chennai 600036, India*

(Received 23 May 2022; accepted 16 September 2022; published 5 October 2022)

Double-perovskite-based magnets wherein frustration and competition between emergent degrees of freedom are at play can lead to novel electronic and magnetic phenomena. In this paper, we report the electronic structure and magnetic properties of an ordered double perovskite material, Ho_2CoMnO_6. In the double perovskites with general class $A_2BB'O_6$ (A = rare-earth ions; B, B' = transition metal ions), the octahedral B and B' sites have a distinct crystallographic site. The Rietveld refinement of x-ray diffraction data reveals that Ho_2CoMnO_6 crystallizes in the monoclinic $P2_1/n$ space group. X-ray photoelectron spectroscopy confirms the charge state of cations present in this material. The temperature dependence of magnetization and specific heat exhibits a long-range ferromagnetic ordering at $T_c \sim 76$ K owing to superexchange interaction between Co^{2+} and Mn^{4+} moments. Furthermore, the magnetization isotherm at 5 K shows a hysteresis curve that confirms the ferromagnetic behavior of this double perovskite. We observed a reentrant glassy state in the intermediate-temperature regime, which is attributed to inherent antisite disorder and competing interactions. A large magnetocaloric effect has been observed much below the ferromagnetic transition temperature. Temperature-dependent Raman spectroscopy studies support the presence of spin-phonon coupling and short-range order above T_c in this double perovskite. The stabilization of magnetic ordering and charge states is further analyzed through electronic structure calculations. The latter also infer the compound to be a narrow-band-gap insulator with the gap arising between the lower and upper Hubbard Co d subbands. Our results demonstrate that antisite disorder and complex 3d-4f exchange interactions in the spin lattice account for the observed electronic and magnetic properties in this promising double perovskite material.

DOI: 10.1103/PhysRevMaterials.6.104401

I. INTRODUCTION

Spin correlations and the interplay between competing degrees of freedom can lead to exotic physical phenomena in novel magnetic materials [1–6]. Transition-metal-and-rare-earth-based magnetic materials are promising candidates to harbor exciting electronic and magnetic properties that could serve as a test bed for establishing theoretical conjectures. In addition, they offer a viable ground to realize the rich potentials of novel magnets with the aim of tailoring the surprising properties of these materials to address the pressing technological challenges in material science in energy harvesting, spintronics, quantum computing, and high-density data storage devices [7–20]. In this regard, the rare-earth double perovskite oxides [21] $A_2BB'O_6$ (A = rare-earth ions or alkaline ions; B, B' = transition metal ions) [22,23] with rocksalt-type ordered structure offer a promising venue in view of their multifunctional properties owing to the coexistence of magnetoelectric coupling, magnetodielectric effects, tunable pyroelectric and ferroelectric properties, multiferroicity, spin-polarized conductivity, and superconductivity [24–26]. Also, double perovskites present a highly flexible structure wherein external perturbations such as chemical pressure and electric and magnetic fields can tune the underlying magnetism and spin dynamics. Furthermore, double perovskites, wherein spin correlations, frustration, and spin-orbit coupling are at play are ideal to realize exotic quantum states such as spin liquid, unconventional magnetic ordering, spin-orbit-driven phenomena, and topological states with emergent excitations [27–33]. Double perovskites are excellent candidates for potential applications such as magnetic memory, sensors, and solar cells, to name a few. For example, the multiferroic material $HoMnO_3$ with a ferroelectric transition and large polarization of 56 mC/m^2 shows a large magnetocaloric effect [34,35].

*nandab@iitm.ac.in
†pkhuntia@iitm.ac.in

 ©2022 American Physical Society

The double perovskites R_2CoMnO_6 (R = rare earth) provide a versatile platform for hosting interesting electronic and magnetic properties which depend on the size of the R ions [36]; for example, the spin-phonon coupling decreases upon replacing La with smaller rare-earth ions. The recent theoretical prediction of multiferroicity in Y_2NiMnO_6 [37] also indicates the significance of the type of rare-earth ion in realizing myriads of complex magnetic ordering phenomena in these double perovskites. The double perovskite materials generally crystallize into two structures, either ordered or disordered, based on the B- and B'-site distinct or mixed occupancy, respectively. The ordered structure prefers to be in the monoclinic space group with $P2_1/n$ symmetry, and the disordered one crystallizes in the orthorhombic space group with *Pnma* symmetry. The ordered double perovskites $A_2BB'O_6$, generally host ferromagnetic (FM) interaction due to superexchange interactions. In contrast, the coexistence of B^{3+} and B'^{3+} ions as a disorder introduces competing antiferromagnetic (AFM) interactions in the spin lattice [38,39]. The magnetic properties of double perovskites are well interpreted following the cationic ordering and Goodenough-Kanamori (GK) rule [40,41], which suggests a ferromagnetic ground state in these systems. The deviations from the GK rule due to cationic disorder lead to the departure from ferromagnetism also. The double perovskites with heavier rare-earth elements show unconventional properties such as magnetization reversal and inverse exchange bias in Er_2CoMnO_6 [42], negative magnetocapacitance in Yb_2CoMnO_6 [43], and anisotropy magnetic properties and a giant magnetocaloric effect in Tb_2CoMnO_6 [35]. Y_2CoMnO_6 shows multiferroic behavior owing to the presence of competing interactions [44], while the steps in the magnetic hysteresis loop are ascribed to antisite disorder in this double perovskite [45,46]. In a similar vein, La_2CoMnO_6 hosts FM ordering and cluster glass phenomena driven by antisite disorder [47]. The unconventional ground states of such double perovskites are the consequence of the B-site cationic ordering and their nominal valence states. Most of the Co-, Ni-, and Mn-based ordered double perovskites exhibit a ferromagnetic (FM) insulating ground state, which is best modeled by the superexchange interactions among the B^{2+} and B'^{4+} ions via adjacent oxygen ions. The complex interplay between $3d$-$4f$ interactions in double perovskites of type R_2CoMnO_6 can lead to rich and diverse physical phenomena such as spin glass, multiferroicity, Griffiths phase, magnetoresistance, exchange bias, and magnetocaloric effect. In these materials, perturbations such as the choice of cations play a crucial role in modifying the underlying electronic and magnetic properties [33]. Double perovskites without disorder are ideal to test theoretical conjectures; however, the experimental realization of such a structure poses a great challenge owing to antisite disorder and defects in real materials. This inspires us to look for new double perovskites with a suitable combination of rare-earth and transition metal ions wherein the disorder could be controlled precisely, providing a viable ground to realize exotic electronic and magnetic phenomena. In this context, the recently synthesized, promising double perovskite Ho_2CoMnO_6 offers an exciting platform to explore complex magnetic ordering and electronic properties. In this material, the Ho^{3+} ion is predicted to impact the FM ordering greatly compared with other double perovskites in view of the smaller atomic radius of the Ho^{3+} ion. In Ho_2CoMnO_6, competition between Co^{2+}-O-Mn^{4+} FM superexchange interaction and Co^{2+}-O-Co^{2+} or Mn^{4+}-O-Mn^{4+} AFM interaction, which are further modulated by the active Ho^{3+} spins, could lead to interesting ground-state properties. A complete picture concerning the exact charge state, electronic structure, exchange interactions, disorder, and spin-phonon coupling is essential to understand the underlying mechanisms that drive novel magnetism in this class of double perovskite materials.

In this paper, we have investigated the structural, magnetic, and electronic properties of the polycrystalline samples of a partially site-ordered double perovskite, Ho_2CoMnO_6 (henceforth referred to as HCMO). The ordered double perovskites of type $A_2BB'O_6$ have two sublattices consisting of BO_6 and $B'O_6$ octahedra, which form a rocksalt-type ordering. The disorders in the form of antisite disorder (ASD), i.e., site exchange between B and B′ ions, which might induce competing exchange interactions in these materials, are unavoidable. HCMO crystallizes in a monoclinic structure with the space group symmetry $P2_1/n$, which is typically found in most of the cation-ordered double perovskite systems. Our x-ray photoelectron spectroscopy (XPS) results reveal the exact charge state of cations in HCMO. The present double perovskite shows a long-range ferromagnetic ordering at around 76 K owing to the Co^{2+}-O^{2-} -Mn^{4+} superexchange interactions. The dc susceptibility, ac magnetization, and specific heat results are consistent with such a phase transition. Moreover, the system reentered in a glassy state (known as the reentrant spin-glass state) below $\simeq$ 37 K, which is manifested as the frequency-dependent broad peak in the ac susceptibility. The observation of this reentrant glassy state could be attributed to inherent antisite disorder and competing interactions in HCMO. Interestingly, HCMO shows a large magnetocaloric effect [the corresponding isothermal magnetic entropy change is found to be $\Delta S_m \simeq 13.5$ J/(kg K) at 15 K] much below the ferromagnetic transition temperature. Raman spectroscopy results point toward the presence of spin-phonon coupling in this novel double perovskite material. The density functional theory calculations are performed on HCMO to find the plausible ground-state magnetic ordering and charge states. A detailed electronic structure analysis establishes the experimentally observed charge states. The ground-state magnetic ordering is found to be AFM2, where the Ho spins form a G-type antiferromagnetic arrangement while the Co and Mn spin sublattices constitute ferromagnetic ordering. However, no particular magnetic ordering between the Ho spins and the Co and Mn spins is observed.

II. EXPERIMENTAL DETAILS

Polycrystalline samples of Ho_2CoMnO_6 was synthesized by the conventional solid-state reaction route using high-purity initial ingredients. At first, stoichiometric amounts of Ho_2O_3 (99.999%; REacton), CoO (99.9995%; Alfa-Aesar), and MnO_2(99.9%; Alfa-Aesar) were mixed well. Then this mixture was pressed into a pellet, placed in an alumina crucible, and heated at 800 °C for 24 h, 900 °C for 48 h, 1000 °C for 48 h, and finally 1250 °C for 60 h, respectively, in a box

furnace with several intermediate regrindings and pelletizations.

Powder x-ray diffraction (XRD) measurements were performed at room temperature with Cu-K_α radiation ($\lambda = 1.541\,82$ Å) on a Rigaku SmartLab diffractometer and were analyzed by the Rietveld method [48] using FULLPROF software [49]. Magnetization measurements were carried out in the temperature range $5.0 \leqslant T \leqslant 370$ K and in the field range $0 \leqslant H \leqslant 70$ kOe using a Quantum Design superconducting quantum interference device–vibrating sample magnetometer (SQUID VSM). For the low-field magnetization measurements, the reset magnet mode option of the SQUID VSM was used to remove any stray or remanent field. Specific heat measurements were performed in the temperature range $1.9 \leqslant T \leqslant 200$ K in zero field using the heat capacity option of a Quantum Design physical property measurement system (PPMS). X-ray photoelectron spectroscopy (XPS) experiments were performed by using a scanning x-ray microprobe system equipped with a monochromatic aluminum K_α x-ray source (1486.6 eV) and a multichanneltron hemispherical electron energy analyzer of the PHI 5000 VersaProbe II Physical Electronics system. The survey scan and core-level spectra were measured at an emission angle of 45° with a pass energy of 50 and 11.750 eV, respectively. The binding energy (B.E.) calibration was done by using C 1s located at 284.6 eV. All the photoelectron measurements were performed inside the analysis chamber with an average base vacuum of 7.0×10^{-10} mbar. A charge neutralizer was used in order to compensate for the surface charging of the samples. The total energy resolution, estimated from the width of the Fermi edge taken from a cleaned polycrystalline gold sample, was about 400 meV for a monochromatic aluminum K_α line with a pass energy of 11.750 eV for the core level. Ar-ion sputtering was performed at 3 keV energy for 30 min with a raster area of $4 \times 4\,\text{mm}^2$. The electronic structure was investigated using XPS valence band spectra. Raman spectra were recorded using a Horiba Jobin Yvon LabRAM HR800 micro-Raman spectrometer equipped with a 473-nm excitation diode laser, 1800 lines/mm grating, an edge filter for Rayleigh line rejection, and a charge-coupled device detector giving a spectral resolution of $\sim 1\ \text{cm}^{-1}$ in backscattering mode. The laser was focused to a spot size of $\sim 1\ \mu$m onto the flat surface of the sample using a 50× objective lens. The low-temperature Raman measurements were performed employing a Janis liquid-He-flow-type cryostat with a temperature stability of ± 0.5 K.

III. RESULTS AND DISCUSSION

A. XRD and crystal structure

We have refined the crystal structure of HCMO using the Rietveld refinement using the FullProf program suite considering the monoclinic space group $P2_1/n$ with a goodness of fit $\chi^2 = 1.24$. The refined lattice parameters obtained from the analysis, $a = 5.2326$ Å, $b = 5.5869$ Å, $c = 7.4737$ Å, and $\beta = 90.12°$, are in excellent agreement with previous reports [50,51]. The Rietveld refinement results are presented in Fig. 1(c), and the resulting atomic coordinates and goodness of Rietveld refinement are summarized in Table I. It is worth mentioning that although the crystal structure is derived from the *Pbnm* perovskite, in the present $A_2BB'O_6$ double perovskite material the symmetry is lower and the Co^{2+} and Mn^{4+} cations are distributed with a 1 : 1 ratio and constitute distinct B sites. Figure 1(a) shows the double perovskite crystal structure of Ho_2CoMnO_6 with MnO_6 and CoO_6 octahedra in a unit cell. Figure 1(b) shows that along the a axis, the Co^{2+}-Co^{2+} and Mn^{4+}-Mn^{4+} ions are constituting a uni-

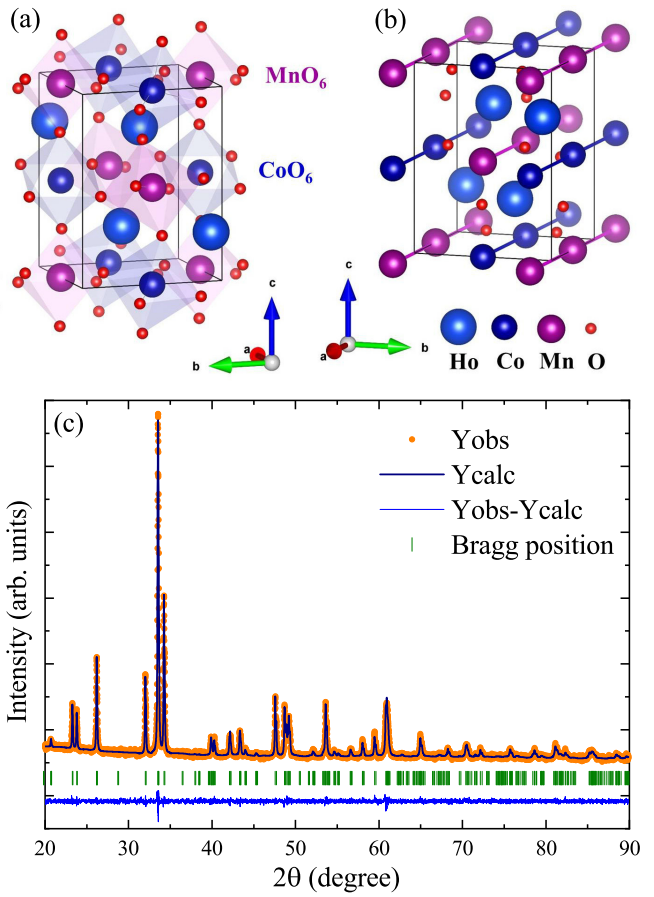

FIG. 1. (a) The double perovskite crystal structure with MnO_6 and CoO_6 octahedra in Ho_2CoMnO_6 in a unit cell. (b) The spins in the chain are interacting along the a axis via Co-Co and Mn-Mn chains with the same bond length, 5.233 Å. (c) The Rietveld refinement of XRD data taken at room temperature.

TABLE I. The crystallographic data of Ho_2CoMnO_6 obtained from Rietveld refinement. The goodness of the Rietveld refinement is defined by the following parameters: profile residual $R_p = 2.30\%$; weighted profile residual $R_{wp} = 2.99\%$; expected profile residual $R_{exp} = 2.69\%$; $\chi^2 = 1.24$.

Atom	Wyckoff position	x	y	z	Occupancy
Ho	4e	0.0203	0.0715	0.2508	1.000
Co	2d	0.0000	0.5000	0.0000	1.000
Mn	2c	0.5000	0.0000	0.000	1.000
O1	4e	0.3180	0.3120	0.0550	1.000
O2	4e	0.3000	0.2880	0.4500	1.000
O3	4e	0.6022	0.9614	0.2380	1.000

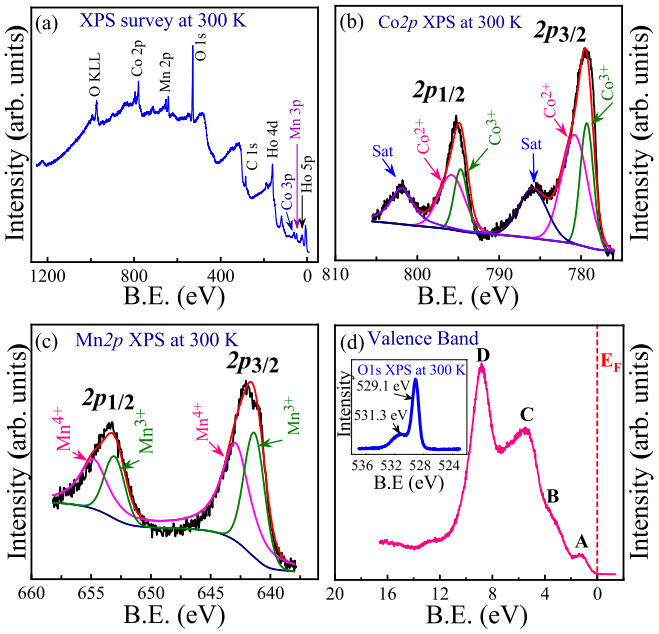

FIG. 2. (a) XPS survey scan of HCMO sample at 300 K. (b) and (c) The core-level XPS spectra of Co 2*p* and Mn 2*p*, respectively. (d) The valence band spectra; the inset shows the core-level spectra of O 1*s*.

form spin chain separately with a minimum bond distance of 5.233 Å. In contrast, the minimum bond distance for cationic neighbors between Co^{2+} and Mn^{4+} ions along the *c* axis [001] is 3.737 Å and along the diagonals in the ab plane [110] is 3.827 Å, respectively. In both directions, Co-Mn pairs are forming a uniform spin chain, and the interaction along one of these directions is most likely the dominant interaction pathway in HCMO. To confirm this scenario, we also performed the electronic structure calculations using density functional theory (DFT).

B. X-ray photoelectron spectroscopy

X-ray photoelectron spectroscopy (XPS) is a powerful technique to probe the valence states and ligand coordination of the constituting elements in any material. In the XPS study of a material having open-shell ions, a core electron vacancy along with the open shell gets coupled to produce the multiple structure. In addition to the main photoelectron peak features, the associated satellite peaks and chemical shifts and their relative intensities are also useful to estimate the oxidation states and ligand coordinations [52,53]. A prior knowledge of the electronic structure of a material is essential to elucidate many of its physical properties. Hence, to understand the electronic structure of the present material, HCMO, we have studied its XPS spectra. All the peak positions have been assigned following the National Institute of Standards and Technology (NIST) database [54]. The deconvolution analysis of the core-level XPS peaks of the relevant ions has been carried out using a combination of Lorentzian and Gaussian distribution functions.

The survey scan XPS spectra recorded at 300 K are shown in Fig. 2(a), which confirms the presence of the elements Ho, Co, Mn, O, and C in the system. The absence of extrinsic elements confirms the sample purity. The observation of the C-1*s* peak is common, and it is attributed to the extrinsic molecules absorbed from the air at the surface.

The core-level Co 2*p* XPS spectrum can provide many pieces of important information, viz., spin state, nominal valence state, etc. [52,53,55,56]. Its shake-up satellite peaks are produced by poorly screened, states whereas the main peaks are originated from the well-screened states. The satellite peaks, in particular, are very sensitive to the valence states of the cobalt ions. Figure 2(b) demonstrates the core-level Co 2*p* XPS spectrum. It comprises two main spin-orbit coupling peaks, i.e., Co $2p_{3/2}$ and Co $2p_{1/2}$ positioned at 779.43 and 795.1 eV, respectively. The two broad peaks situated above the main peaks are assigned as the charge transfer satellite peaks. Eventually, such prominent satellite peaks above the main peaks are typically observed in Co 2*p* XPS spectra of the materials containing divalent Co^{2+} ions, while such satellite peaks are merely absent or very weak for systems having trivalent Co^{3+} ions [52,53,55]. Hence the observation of the satellite peaks in the present Co 2*p* XPS spectrum indicates the presence of Co^{2+} ions in HCMO. It is worth mentioning here that the asymmetry and broadening of the observed peaks are indicative of the presence of mixed valence states of the Co ions [53,55,56]. The peak positions and line shape of the observed Co 2*p* XPS spectrum are similar to the earlier reports showing mixed valence Co ions [53]. Again, the doublet separation between the spin-orbit coupling peaks is typically found to be 15.9 eV for CoO and 15.3 eV for Co_2O_3. For the present system, the Co 2*p* doublet separation is observed to be 15.6 eV, which suggests for the existence of both Co^{2+} and Co^{3+} ions. The Co 2*p* XPS spectrum has been deconvoluted to estimate the concentrations of different Co ions (Co^{2+} and Co^{3+}) as shown in Fig. 2(b). Although Co^{2+} ions are found to be predominantly present in the system, the presence of Co^{3+} ions is also unavoidable. This in turn can give rise to competing exchange interactions in HCMO.

The core-level Mn 2*p* XPS spectrum of the present material is depicted in Fig. 2(c). This spectrum is broadly divided into two spin-orbit coupling peaks, i.e., Mn $2p_{3/2}$ and Mn $2p_{1/2}$, which are observed at 641.7 eV and 653.4 eV, respectively. The values of the Mn $2p_{3/2}$ peak positions in compounds Mn_2O_3 and MnO are reported to be 641.3 eV and 642.2 eV, respectively [54]. Hence the observed value of the Mn $2p_{3/2}$ peak position in HCMO suggests the existence of mixed valence states of Mn ions (Mn^{3+} and Mn^{4+}). For the present system, the spin-orbit splitting energy (ΔE) in the Mn 2*p* XPS spectrum is found to be $\simeq$ 11.7 eV. On the other hand, ΔE for MnO_2 and Mn_2O_3 are reported to be 11.8 and 11.6 eV, respectively. Thus the observed intermediate value of $\Delta E \simeq$ 11.7 eV can be presumably attributed to the mixed oxidation states of Mn ions (Mn^{3+} and Mn^{4+}) [53]. The deconvolution analysis of the Mn 2*p* XPS peaks and the concentrations of the relevant Mn^{3+} and Mn^{4+} ions are depicted in Fig. 2(c). The O 1*s* core-level XPS spectrum is illustrated in the inset of Fig. 2(d), which comprises two peaks. The most intense peak at 529.1 eV can be ascribed to the O^{2-} ions, while the smaller broad peak at 531.3 eV is known to be associated with the less-electron-rich oxygen species (viz., O_2^{2-}, O_2^{-},

or O^-) owing to the adsorption of oxygen at the surface [52,53].

The valence band (VB) XPS spectrum is illustrated in Fig. 2(d). It is clear from Fig. 2(d) that no electronic states are available near the Fermi level (E_F), which is a clear indication of the insulating nature of HCMO. The observed VB spectrum is made up of four peaks marked as features A, B, C, and D. The first spectral feature, feature A, lying immediately below the Fermi energy (0–1 eV), can be attributed to the extended hybridized states of Co $3d$ (e_g) and Mn $3d$ (e_g) [52,53]. The next two features, marked as features B and C, can be primarily attributed to the hybridization of states of Mn $3d(t_{2g})$, Co $3d(e_g)$, and Ho $4f$ along with O $2p$ states [52,53]. The last peak in the VB spectrum, denoted as feature D, is seemingly related to the hybridization of the extended Mn $3d(e_g)$ and Co $3d(e_g)$ states with O $2p$ states, while some other minor contributions are owing to the O-$2p$–(Co or Mn)-$4sp$ and O-$2p$–Ho-$5sd$ oxygen bonding states [52,53].

C. Magnetization and specific heat

In HCMO, one expects competing exchange interactions due to the presence of three different magnetic ions with different energy scales of interactions in the spin lattice with inevitable disorder. The competing interactions may drive the system towards an unconventional magnetic state. In order to probe the ground-state magnetic proprieties of this material, we measured the dc magnetization $M(T)$ as a function of temperature on a hard pellet of HCMO in zero-field-cooled (ZFC) and field-cooled (FC) modes in several magnetic fields H using a Quantum Design SQUID VSM. The magnetic susceptibility data show a paramagnetic behavior at high temperature and an anomaly at ~ 76 K suggesting the presence of a magnetic phase transition [Fig. 3(a)].

Similarly to the previous magnetization study on HCMO [51], the susceptibility data were fitted with the Curie-Weiss (CW) law given by the equation $\chi^{-1} = (\chi_0 + \frac{C_{RE}}{T-\theta_{RE}} + \frac{C_{TM}}{T-\theta_{TM}})^{-1}$, where χ_0 is the temperature-independent susceptibility (arising from the core diamagnetic and paramagnetic Van Vleck contributions) and C_{RE} (C_{TM}) and θ_{RE} (θ_{TM}) are the Curie constant and the Curie-Weiss temperature for rare-earth (transition metal) ions, respectively. In HCMO, the magnetic properties are governed by both rare-earth Ho^{3+} ($4f^{10}$, $^5I_8$; $J = 8$) ions and transition metal ions (Co^{2+} and Mn^{4+}). The main features of our observations from the magnetization measurement are described below. The material shows a long-range FM ordering around 76 K due to the superexchange interaction between Co^{2+} (t_{2g}^5, e_g^2) and Mn^{4+} (t_{2g}^3, e_g^0) magnetic moments. From the CW fit, we obtained $\theta_{RE} = -4.2$ K, $\theta_{TM} = 79.4$ K. The small and negative value of θ_{RE} suggests the presence of a weak antiferromagnetic interaction between Ho^{3+} moments and the sublattice consisting of transition metal ions Co^{2+} and Mn^{4+} or associated with the crystal electric field excitations of the $^5I_8$ multiplet of the Ho^{3+} ion. Ho^{3+} moments may undergo a phase transition at lower temperature below 2 K. Whereas, the positive value of θ_{TM} indicates a ferromagnetic interaction between Co^{2+} and Mn^{4+} in the host spin lattice. The presence of AFM and FM interactions suggests that HCMO hosts a frustrated spin lattice. The obtained effective magnetic

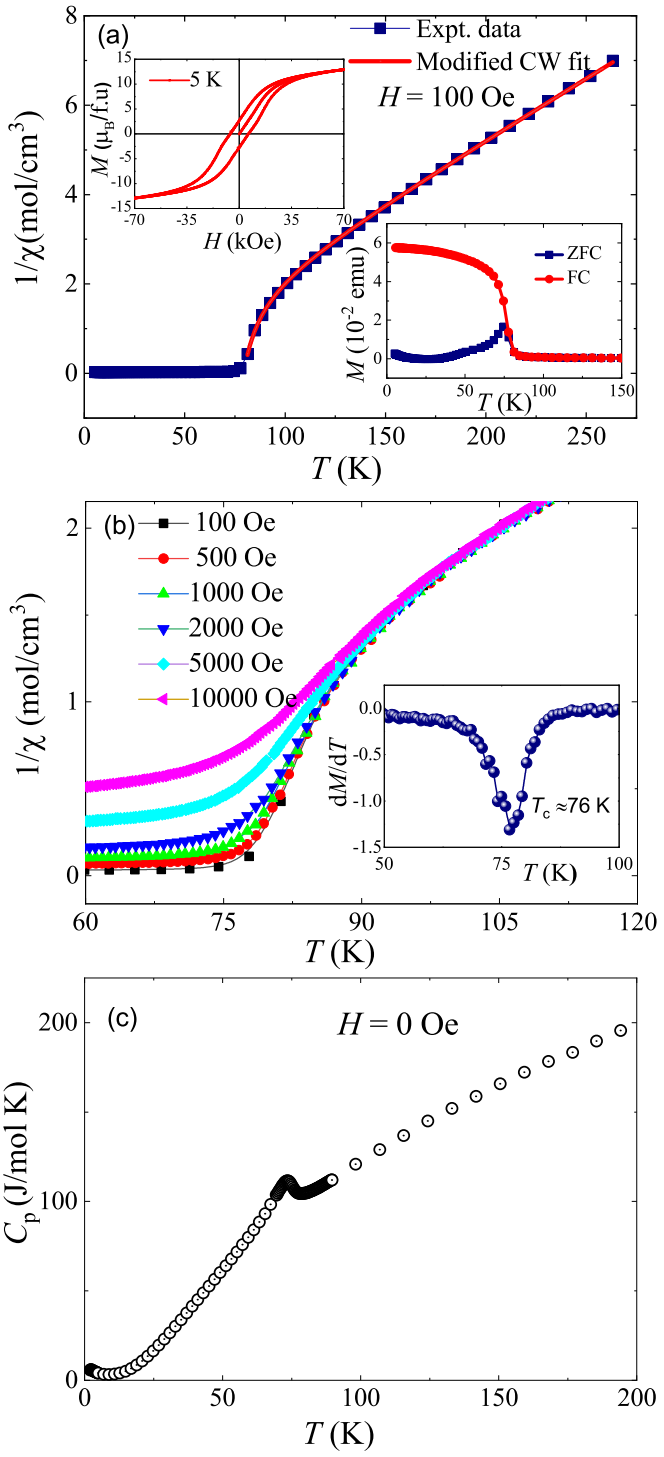

FIG. 3. (a) The temperature dependence of inverse magnetic susceptibility in an applied magnetic field of 100 Oe. The upper inset depicts the $M(H)$ loop at 5 K reflecting FM order in HCMO. The lower inset shows a closer view of the temperature dependence of magnetization recorded in ZFC-FC modes in 100 Oe, which shows a bifurcation at $T = 76$ K. (b) The temperature dependence of $1/\chi$ in different magnetic fields. The inset shows the derivative of magnetization (dM/dT) vs T taken in FC mode in an applied magnetic field of 500 Oe clearly depicting an anomaly at 76 K. (c) The temperature dependence of specific heat of HCMO in zero field. A peak around 73.4 K is due to the long-range ordering.

moment ($\sqrt{8C}\mu_B$) for transition metal cations is 5.44 μ_B. This value of μ_{eff} is close to the theoretically expected value ($\mu_{eff} = \sqrt{\mu^2_{eff}(Co^{2+}) + \mu^2_{eff}(Mn^{4+})}$ for the Co^{2+} ($3d^7$, $S = 3/2$) and Mn^{4+} ($3d^3$, $S = 3/2$) sublattice system [$(\mu_{eff})_{theo} = 5.47\ \mu_B$/f.u.]), indicating the presence of divalent Co and tetravalent Mn sublattices, respectively [57]. The effective moment for the rare-earth ion Ho^{3+} in HCMO is 11.03 μ_B, which is a bit larger than that expected for the free Ho^{3+} ion but is consistent with previous reports [51]. The finding that the value of the Ho^{3+} magnetic moment is a bit larger compared with the free-ion value possibly indicates a weak interaction between Ho^{3+} and the Co and Mn sublattices. Figure 3(b) shows the temperature dependence of inverse susceptibility data in different applied magnetic fields displaying a phase transition around 76 K. The inset of Fig. 3(b) shows the derivative of magnetization (dM/dT) vs T taken in FC mode in 500 Oe clearly depicting an anomaly at 76 K owing to FM order. Furthermore, the magnetic hysteresis behavior of magnetization $M(H)$ at 5 K [see the upper inset of Fig. 3(a)] confirms the presence of FM order. The behavior of inverse magnetic susceptibility above T_c is most likely due to the persistence of short-range spin correlations in this double perovskite.

The bifurcation of the ZFC-FC data below $T_c = 76$ K in an applied field of 100 Oe, as shown in the lower inset of Fig. 3(a), indicates the presence of a spin-glass [58] state in HCMO. The FC magnetization increases upon lowering the temperature below the transition temperature and tends to saturate at low temperature indicating the polarization of $4f(Ho^{3+})$ moments in an applied magnetic field. In order to gain further insight into the magnetic ordering and the low-energy excitations in HCMO, we measured the specific heat of HCMO at constant pressure $C_P(T)$ in the T range $1.9 \leqslant T \leqslant 200$ K in zero field. The sharp anomaly at around 73.4 K in the $C_p(T)$ vs T data supports the presence of a long-range FM ordering as observed in the dc magnetization. However, there is a little discrepancy between the T_c observed in magnetization and specific heat experiments. The finding that the value of T_c is a bit higher in the magnetization experiments is most likely due to the fact that the transition temperature T_c is quite sensitive to the magnetic field used for magnetization measurements, while the specific heat was measured in zero field. Another plausible scenario regarding the slight discrepancy in T_c observed by magnetization and specific heat measurements could be due to the fact that dissimilar experimental techniques track a bit different spin dynamics. This small difference in T_c measured by dissimilar experimental techniques is also observed in other frustrated magnets (see, for instance, Ref. [59]); however, the exact origin of this difference is not clear at present. The enhancement of specific heat below 5 K [see Fig. 3(c)] suggests the onset of a phase transition at much lower temperature owing to a weak exchange interaction between Ho^{3+} moments.

D. ac susceptibility

The splitting of ZFC and FC curves below ~ 76 K suggests that a spin-freezing mechanism is at play which could be associated with antisite disorder and frustration in HCMO. The ac susceptibility is a very sensitive probe to track the spin-freezing mechanism and shed insight into the characteristics of magnetization dynamics in the ordered state of frustrated magnets. Generally, the spin dynamics slow down below the freezing temperature T_f owing to the cluster formation of spin domains. In order to confirm the dc susceptibility results and understand the glassy behavior of this frustrated magnet, we performed ac susceptibility measurements at several frequencies. Figure 4(a) depicts the imaginary part of the ac susceptibility [$\chi''(T)$], which shows a sharp peak at the FM ordering temperature $T_c = 76$ K and a broad maximum around $T_f = 30$ K. The maximum at $T_f = 30$ K shifts towards higher temperature upon increasing the frequency indicating a glassy spin dynamics leading to a slow relaxation of magnetization. To investigate the variation of T_f with frequency, we have analyzed it following the scaling law relevant for critical dynamics [60,61] given by

$$\tau = \tau_0 \left(\frac{T_f - T_0}{T_0} \right)^{-zv}. \quad (1)$$

Here, T_f is the freezing temperature [f is the corresponding frequency for which $\chi''(T)$ attains a maximum], T_0 is the equivalent spin-glass freezing temperature when $f \to 0$ Hz and $H_{dc} \to 0$ Oe, and τ_0 is related to the characteristic spin flipping time ($f_0 = \frac{1}{\tau_0}$); zv is the dynamical critical exponent. Figure 4(b) shows the critical dynamic scaling fit. The best fitting yields $\tau_0 = 10^{-8}$ s, $T_0 = (29.3 \pm 0.2)$ K, and $zv = (5.29 \pm 0.04)$, which is in reasonable agreement with the values expected for a cluster spin-glass state ($4 < zv < 12$). For a canonical spin-glass system, τ_0 lies between 10^{-12} and 10^{-13} s, which is smaller than the observed value of 10^{-8} s by a few orders. The longer relaxation time τ_0 indicates that the spin-freezing characteristic is of cluster-glass type rather than atomic.

To explore further the characteristics of intercluster interactions, the well-known Vogel-Fulcher (VF) model [see Eq. (2)] was employed for fitting the relaxation time τ vs T_f curve. Figure 4(c) shows the corresponding VF model fit.

$$\tau = \tau_0 \exp\left(\frac{E_A}{k_B(T_f - T_0)} \right), \quad (2)$$

where T_0 represents the intercluster interaction strength and E_A is the activation energy required to overcome the barrier of the metastability of the spin-glass (SG) state. The best fitting yields $\tau_0 = 10^{-7}$ s, $T_0 = (26.8 \pm 0.1)$ K, and $E_A/k_B = (53.1 \pm 0.4)$ K. The large value of τ_0 is expected from interacting magnetic spin clusters. All the features observed from ac magnetization results point towards the stabilization of a reentrant spin-glass (RSG) ground state below $T_f = 30$ K.

We also measured the isotherm magnetization at several temperatures, and Fig. 5(a) shows the corresponding plot. As depicted in Fig. 5(a), the magnetization increases upon increasing the external magnetic field and does not saturate up to 7 T. Using the magnetic isotherm data around T_c, we have created a modified Arrott plot [62,63] considering the mean-field model (where the critical exponents are $\beta = 0.5$ and $\gamma = 1$), which corroborates the presence of ferromagnetic order in this material. Figure 5(b) represents the corresponding Arrott plot with a set of parallel lines near $T_c = 76$ K in high field. The nonlinear behavior of the Arrott curves suggests the presence

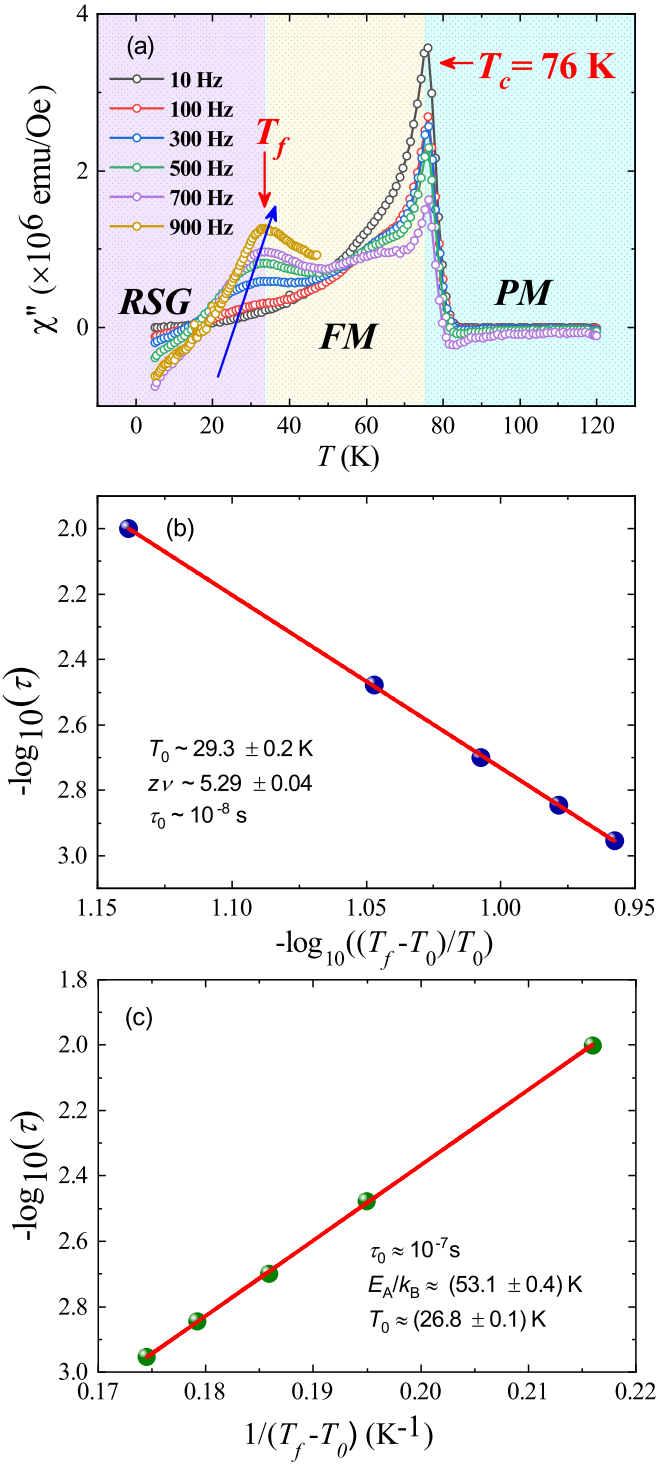

FIG. 4. (a) The temperature dependence of the imaginary part of the ac susceptibility χ'' data at different frequencies with an applied ac field of 3.5 Oe. PM corresponds to paramagnetic phase. The inverse of the frequency vs freezing temperature T_f data is fitted (b) with the critical slowing-down model and (c) with the Vogel-Fulcher law.

of inhomogeneous magnetism possibly related to the fact that the unavoidable disorder strongly affects the underlying spin dynamics of HCMO [64].

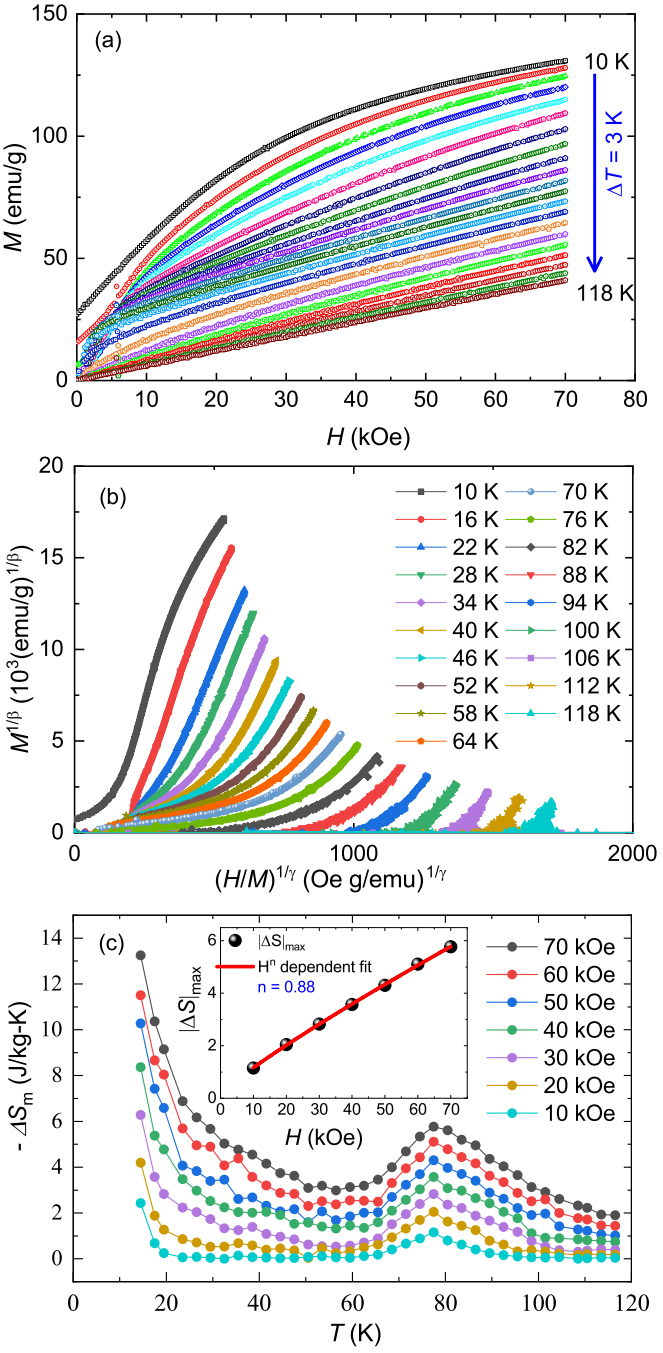

FIG. 5. (a) Magnetization isotherms at several temperatures. (b) The modified Arrott plot of isotherm magnetization following mean-field approximation. (c) The magnetic entropy change, $-\Delta S_m$, as a function of temperature showing a peak at FM ordering temperature with $T_c = 76$ K. The inset shows the maximum value of magnetic entropy change $|\Delta S_m|_{max}$ vs H with a power-law fit as represented by a solid red line.

External perturbations such as magnetic field play a crucial role in modifying the ground-state properties and internal energy of the double-perovskite-based magnetic material under study [65]. The temperature variation in magnetic materials leading to change in entropy due to an adiabatic change in the external magnetic field is known as the magnetocaloric effect and is relevant for magnetic refrigeration [66,67].

Geometric frustration plays an important role in the enhancement of the change in magnetic entropy in the presence of a magnetic field, which in turn can lead to a large magnetocaloric effect in double perovskites [68]. In order to extract the temperature dependence of the change in magnetic entropy in HCMO, we have measured magnetization isotherms at several temperatures. For the characterization of the magnetocaloric response of a material, three main parameters can be studied: the isothermal magnetic entropy change ΔS_m, the adiabatic temperature change ΔT_{ad}, and the refrigerant capacity. Generally, ΔS_m can be calculated indirectly from the experimental magnetization curves using Maxwell's relation.

$$\Delta S_m = \mu_0 \int_0^H \left(\frac{\delta M}{\delta T}\right)_H \delta H. \tag{3}$$

The resulting temperature dependence of the magnetic entropy change ΔS_m in different applied magnetic fields is shown in Fig. 5(c). In ferromagnetic materials, the magnetic field aligns the moments along the field direction by overcoming the thermal fluctuations, leading to a decrease in the magnetic entropy change, $\Delta S_m < 0$. In contrast, the external magnetic field plays a vital role in rotating the spins against their preferential directions yielding an increase in magnetic entropy, $\Delta S_m > 0$, in antiferromagnetic materials [69,70]. As depicted in Fig. 5(c), a peak in $-\Delta S_m$ around T_c corroborates a phase transition from a paramagnetic state to a ferromagnetically ordered state. The value of ΔS_m increases upon lowering the temperature and attains a maximum value of $\sim$13.5 J/(kg K) at low temperature in a magnetic field of 7 T. The enhancement of $-\Delta S_m$ at low temperature indicates the onset of a magnetic ordering most likely due to the presence of a weak exchange interaction between Ho^{3+} moments. As presented in Fig. 5(c), HCMO shows a large magnetocaloric effect [the corresponding isothermal magnetic entropy change is found to be $\simeq$ 13.5 J/(kg K) at around 15 K] much below the ferromagnetic transition temperature [51]. The obtained large value of magnetic entropy change owing to adiabatic demagnetization is quite unusual in double perovskites, which suggests that HCMO is a promising candidate for magnetic refrigeration technology. Furthermore, the variation of the maximum value of entropy change, i.e., $|\Delta S_m|_{max}$, with the magnetic field obeys a power law ($\propto H^n$) reflecting a second-order phase transition, where n is a temperature-dependent parameter [71]. As shown in the inset of Fig. 5(c), the power-law fit yields a magnetic ordering parameter $n = 0.881$, which is close to the value obtained in another double perovskite, Dy_2CoMnO_6 [72]. The value of the exponent n is related to the critical exponents (β and γ) near the T_c, and it is defined as $n = 1 + \frac{(\beta-1)}{(\beta+\gamma)}$ [73]. The obtained value of the parameter n indicates that the magnetic order in HCMO might be best described by modified Arrott plots, viz., the three-dimensional (3D) Heisenberg model, the 3D Ising model, or the tricritical model, rather than by the mean-field framework, which invokes the need for further studies.

E. Raman spectra

The complex interplay between emergent degrees of freedom can lead to interesting magnetic phenomena in double perovskites. Raman spectroscopy is an ideal probe to track competing magnetic ordering phenomena and exotic collective excitations in correlated quantum magnets. This technique has been very successful in revealing interesting insights into the phonon characteristics and spin-phonon coupling of many interesting perovskite-based oxide materials [74–76]. In order to understand the coupling between spin and phonons in HCMO, we measured Raman spectra down to 10 K. The Raman spectra are presented in Fig. 6(a), which shows the most prominent Raman band at 635 cm^{-1} and another less intense band at 515 cm^{-1}. As the less intense Raman band at 515 cm^{-1} is not shifting that much with temperature, we focused our data and analysis at the 635 cm^{-1} band. We have fitted each Raman spectrum with a Lorentzian peak profile (shown for a few selected temperatures) to determine the exact peak position and the full width at half maximum as well. Figure 6(b) shows a plot of the temperature dependence

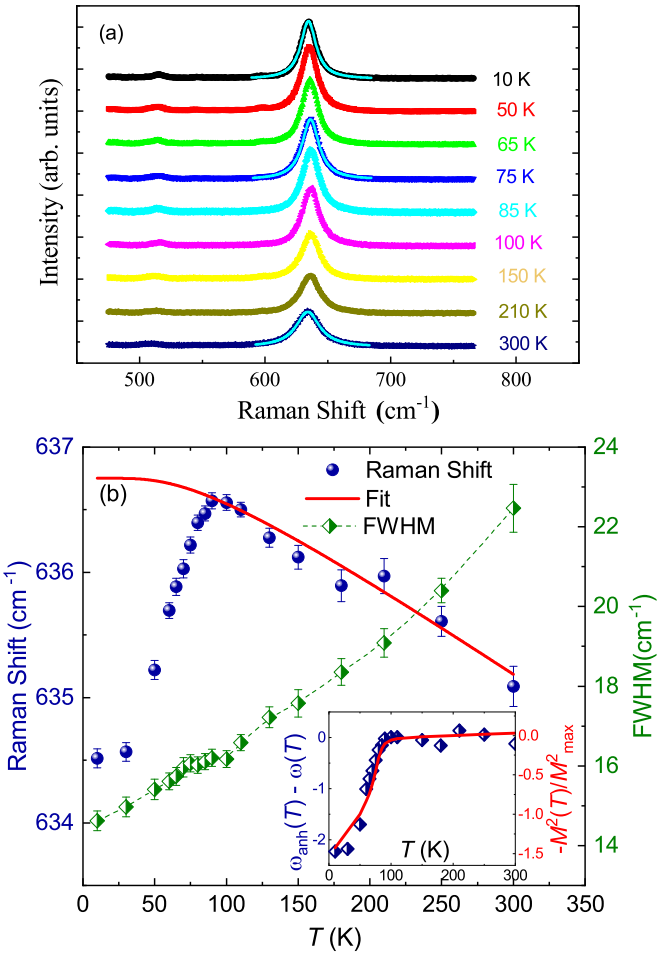

FIG. 6. (a) Raman spectra with Lorentzian fit at a few selected temperatures. (b) The anharmonic nature of the prominent Raman band (635 cm^{-1}) as a function of temperature. The solid red line represents the standard $\omega_{anh}(T)$ dependence expected in the absence of spin-phonon coupling. The variation of the full width at half maximum (FWHM) with temperature is shown on the right y axis. The inset shows that the departure from the anharmonic behavior $\Delta\omega(T)$ of the prominent Raman band is commensurate with the normalized magnetic moment $M^2(T)/M^2_{max}$, where temperature is an implicit parameter.

of the Raman shift. The Raman shift increases upon decreasing the temperature, and this shift suddenly drops below 85 K, which indicates the dominant role of ferromagnetic ordering in phonon frequencies in this material. Such a temperature dependence of the Raman shift could be associated with (i) the anharmonic frequency shift at constant volume, as proposed by Balkanski *et al.* [77] in the absence of structural phase transitions, and (ii) spin-phonon coupling. The anharmonicity of phonon modes can be represented by the following relations:

$$\omega_{\text{anh}}(T) = \omega_0 - C[1 + 2/(e^{\hbar\omega/k_BT} - 1)], \tag{4}$$

$$\Delta\omega(T) = \omega_{\text{anh}}(T) - \omega_0 \propto \frac{M^2(T)}{M^2_{\text{max}}}, \tag{5}$$

where ω_0 and C are adjustable parameters. At high temperature, the Raman shift of the most intense Raman band at 635 cm^{-1} follows the anharmonic behavior as shown in Fig. 6(b). A noticeable deviation of the Raman shift around 85 K suggests the softening of phonon modes associated with spin-phonon interactions possibly due to stretching of CoO_6 and MnO_6 octahedra in HCMO. Such behavior of the Raman shift around 85 K is known to occur due to the spin-phonon coupling ascribed to the role of lattice vibrations in tuning the exchange integral in a magnetic material. The onset of softening of phonon modes around 85 K indicates the existence of short-range ordering which is consistent with our magnetization results. It is worth mentioning that this type of magnetic-order-induced renormalization of phonon frequencies [74,75] has been observed in several double perovskites such as La_2CoMnO_6 [76] and Ba_2NiMnO_6 [78]. Understanding the role of competing magnetic order and spin correlations in tuning the phonon frequencies in double perovskites is an interesting setting in the context of novel material design. As per the phenomenological model employed in Refs. [74,75], the effect on the phonon of a renormalization of electronic states in the proximity of FM order is proportional to the spin-spin correlation of the localized nearest-neighbor spins. In the mean-field approximation, the spin-spin correlation between Co^{2+} and Mn^{4+} spins is proportional to $M^2(T)/M^2_{\text{max}}$ in the present double perovskite, where $M(T)$ represents the average magnetization per magnetic ion at a temperature T. Below 85 K, $\Delta\omega(T)$ closely follows relation (5), which is shown in the inset of Fig. 6(b). Our Raman results rule out the presence of a structural phase transition as evidenced by the absence of remarkable features in the Raman spectra of HCMO in the temperature range of investigation, which is consistent with specific heat and previous neutron scattering studies [50]. The existence of spin-phonon coupling suggests that there is an innate connection between magnetism and the lattice in this $3d$-$4f$ double perovskite.

F. Electronic and magnetic structure of HCMO from density functional theory calculations

In order to gain further insight into the experimentally observed charge and magnetic configurations, density functional theory (DFT) calculations were carried out to find the ground-state electronic and magnetic properties of HCMO. The calculations were carried out on five magnetic configurations, namely, FM, AFM1, AFM2, AFM3, and AFM4 (see Fig. 7). For this purpose, we considered the experimentally obtained crystal structure and used the projector augmented wave (PAW) [79] method as implemented in the Vienna *ab initio* simulation package (VASP) [80]. The generalized gradient approximation (GGA) was chosen for the exchange-correlation functional. The effect of strong correlation was incorporated via the effective interaction parameter $U_{\text{eff}} = U - J$ through the rotationally invariant Dudarev's approach [81]. The Brillouin zone integration was carried out using $8 \times 8 \times 4$ and $12 \times 12 \times 6$ k meshes to achieve self-consistency and to obtain the density of states (DOS), respectively. The PAW basis functions include $2s$ and $2p$ orbitals for O; $4f$, $5d$, and $6s$ orbitals for Ho; and $3d$ and $4s$ orbitals for Co and Mn.

To examine the magnetic structure, we have designed various magnetic configurations, which are depicted in Fig. 7(a). In these configurations, various antiferromagnetic arrangements have been considered on Ho such as A type (AFM1), G type (AFM2), and C type (AFM4) while keeping ferromagnetic interaction between Co and Mn, whereas in one of the configurations (AFM3), the Ho-Ho interaction is maintained to be ferromagnetic while keeping the G-type antiferromagnetic arrangement for Co and Mn. In Table II, we list the relative energies of the five magnetic configurations as a function of U_{eff} for two cases: For the first case the on-site correlation strength is varied uniformly on Co and Ho ($U_{\text{Mn}} = 0$), whereas for the second case a moderate value is fixed on Mn ($U_{\text{eff}} = 2$ eV) while varying U_{eff} uniformly on Ho and Co. A primary electronic structure analysis of the spin-polarized GGA DOS ($U_{\text{eff}} = 0$) [see inset in Fig. 7(b)] suggests that the exchange splitting for Mn is nearly the same as the crystal field splitting ($\Delta_{\text{ex}} \approx \Delta_{\text{cr}}$) [82]. As a result, there are no partially occupied states at the Fermi level, and a gap exists even without considering the on-site correlation effect. On the other side, for Co, $\Delta_{\text{ex}} > \Delta_{\text{cr}}$ and the Fermi level is partially occupied with the down-spin channel of the t_{2g} manifold which gives rise to metallicity in the system. Therefore finite correlation strength is required on Co to open up a gap, whereas U_{eff} on Mn is hardly required. Furthermore, the robustness of the magnetic structure is also analyzed for a moderate value of U_{eff} (=2 eV) on Mn.

As inferred from Table II, under an independent electron approximation (GGA) a FM ground state is preferred, which is contrary to the experimentally reported Curie-Weiss behavior where the negative value of θ_{RE} infers an antiferromagnetic ground state. Often such a discrepancy in magnetically active transition metal oxides arises due to the lack of an appropriate measure of the strong correlation effect. In this regard as discussed earlier we have carried out GGA+U calculations that reveal that the AFM2 configuration, where Ho stabilizes G-type ordering while Co and Mn possess ferromagnetic ordering, forms the ground state. Due to the $P2_1/n$ crystal symmetry, the configurations that allow the magnetic coupling between Co or Mn spins and Ho spins are FM and AFM3. However, as AFM2 constitutes the ground state, the Ho spins remain uncoupled to those of Co and Mn. Furthermore, we find that any kind of antiferromagnetic ordering among Co and Mn results in a higher-energy configuration. For example, the configuration AFM3, where nearest-neighbor Co and

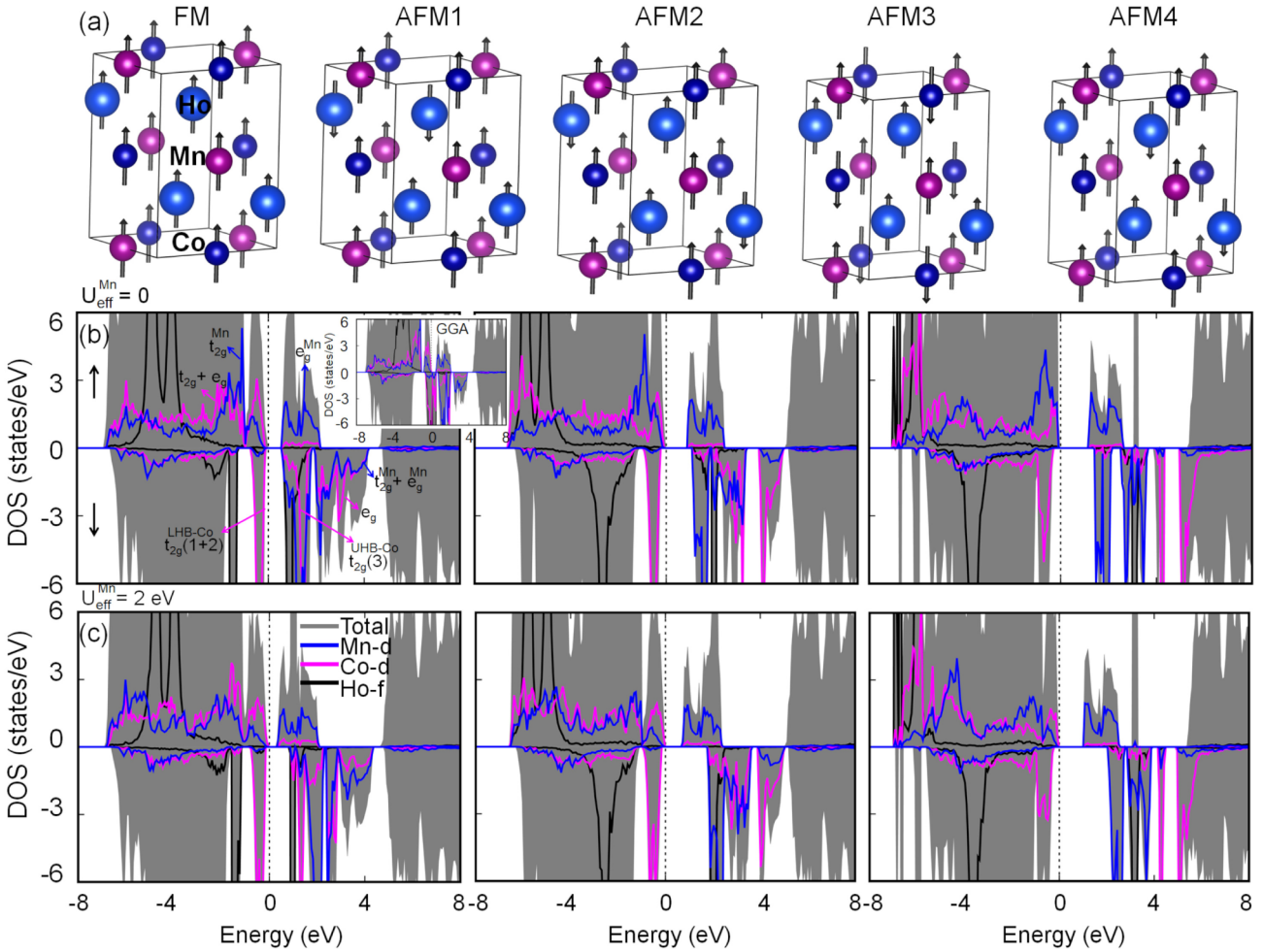

FIG. 7. (a) The five considered magnetic arrangements, namely, ferromagnetic (FM), antiferromagnetic 1 (AFM1), AFM2, AFM3, and AFM4, respectively. The AFM1, AFM2, and AFM4 configurations are designed in such a way that Ho atoms form A-type, G-type, and C-type antiferromagnetic arrangements, whereas in the AFM3 configuration the Co and Mn atoms form G-type arrangements while keeping ferromagnetic interaction between Ho atoms. (b) The spin- and atom-resolved DOS of the most stable magnetic configuration, AFM2, as a function of U_{eff}. The U_{eff} is varied uniformly on Ho and Co (U_{eff} = 2, 4, and 6 eV) atoms while it is kept at zero for Mn. The inset depicts the DOS for the GGA case. (c) The variation in DOS by keeping U_{eff} fixed on Mn while varying U_{eff} on Ho and Co.

Mn are antiferromagnetically oriented, is at least two orders higher in energy as compared with the ground state. This further validates the positive value of θ_{TM}, suggesting FM interaction as obtained experimentally.

The local magnetic moments listed in Table II along with the orbital-projected DOS, shown in Fig. 7, describe the electronic and magnetic structure of HCMO. As can be clearly seen, for Mn, irrespective of U_{eff}, in the majority spin channel

TABLE II. The relative energy differences E_{rel} in meV/f.u. with respect to the most stable magnetic configuration (config.) and corresponding local spin magnetic moments at Ho, Co, and Mn in μ_{B}. The unbracketed and bracketed terms in E_{rel} represent the relative energies without and with considering U_{eff} on Mn.

	GGA				GGA+U											
	U = 0				U_{eff} = 2 eV				U_{eff} = 4 eV				U_{eff} = 6 eV			
Config.	E_{rel}	Ho	Co	Mn	E_{rel}	Ho	Co	Mn	E_{rel}	Ho	Co	Mn	E_{rel}	Ho	Co	Mn
FM	0	3.81	2.30	2.90	18.15 (8)	3.92	2.45	2.90	16.27 (6.25)	4	2.57	2.88	13.7 (4.37)	4.15	2.78	2.81
AFM1	72.734	3.80	2.20	2.94	39.84 (28.55)	3.90	2.50	2.80	35.42 (15.27)	3.98	2.70	2.7	33.19 (7.52)	4.05	2.85	2.83
AFM2	72.87	3.82	2.22	2.92	0	3.92	2.45	2.92	0	4	2.58	2.88	0	4.1	2.79	2.82
AFM3	210.2	3.82	2.40	2.82	117.04 (220.25)	3.92	2.52	2.9	96.45 (289.2)	4	2.62	2.85	64.8 (345.7)	4.13	2.81	2.85
AFM4	83.56	3.8	2.35	2.94	14.43 (10.58)	3.92	2.43	2.91	21.08 (13.55)	4	2.6	2.88	26.28 (15.81)	4.13	2.78	2.82

the t_{2g} states are occupied and the e_g states are empty, whereas in the minority spin-down channel the d states are completely unoccupied inferring a 4+ charge state with the 3-μ_B spin moment arising from the $t_{2g}^{3\uparrow} e_g^0$ electronic configuration. For Co and Ho, the d and f states are completely occupied in the majority spin channels while in the spin minority channel they are partly occupied highlighting the 2+ and 3+ charge states with $t_{2g}^{3\uparrow} t_{2g}^{2\downarrow} e_g^{2\uparrow}$ and $f^{7\uparrow 3\downarrow}$ electronic configurations. The on-site repulsion due to strong electron correlation creates a lower Hubbard band and an upper Hubbard band (LHB and UHB) in the minority Co d spectrum, as shown in Fig. 7(b), to create a narrow-band-gap insulating system. The charge states inferred from the electronic structure analysis are in very good agreement with the experimentally observed charge states from the XPS measurements. The stabilization of the Co^{2+} and Mn^{4+} electronic configurations in the octahedral environment matches with the hypothesis proposed by Parida *et al.* [82] and demonstrates the case where the exchange field is comparable to or greater than the crystal field split.

IV. CONCLUSIONS

We synthesized high-quality polycrystalline samples of the double perovskite Ho_2CoMnO_6, which crystallizes in the monoclinic $P2_1/n$ space group. X-ray photoelectron spectroscopy unveils the exact charge state of cations in this material. The magnetic hysteresis curves $M(H)$ at 5 K confirm a FM state owing to superexchange interaction between $3d$ moments Co^{2+}-O-Mn^{4+}. The specific heat confirms the presence of ferromagnetic long-range ordering. The bifurcation of ZFC-FC curves at $T_c = 76$ K in low field, $H = 100$ Oe, indicates the presence of spin freezing in this double perovskite material, which is also supported by the frequency-dependent ac susceptibility data. Also, the Vogel-Fulcher and critical slowing model fits point towards the stabilization of a reentrant spin-glass ground state below $T_f = 30$ K as the spin flipping has a longer relaxation time compared with a conventional spin glass. The presence of competing interactions and antisite disorder leads to such a spin-glass state in HCMO. In addition, magnetization results suggest the existence of a disordered state and short-range spin correlations above T_c in this material. The temperature-dependent Raman spectra support the magnetization results. Our Raman spectroscopy results suggest that there is a significant contribution of spin-phonon coupling in the magnetically ordered state that arises from the phonon-mediated modulation of the exchange integral in this material. The presence of spin-spin correlations is manifested by the deviation of the spectral line shift from its anharmonic nature around 85 K. The relatively large value of magnetocaloric entropy change, $\Delta S_m \simeq 13.5$ J/(kg K), much below the ferromagnetic ordering temperature, suggests that HCMO is a promising candidate for magnetic refrigerant applications. The electronic structure calculations corroborate the experimentally observed charge states and provide insight into the magnetic ordering in this double perovskite. The ground-state magnetic ordering is found to be the one where the Ho spins form a G-type antiferromagnetic arrangement while the Co and Mn spin sublattices constitute ferromagnetic ordering. Furthermore, our calculations reveal that the present double perovskite is a narrow-band-gap insulator, which is consistent with XPS results. Due to the strong correlation effect in the spin minority channel, the Co-t_{2g} manifold splits into lower and upper Hubbard subbands to create a narrow gap. The spin majority channel has a natural band gap due to the crystal field split of the Mn d states. Further studies are desired to understand the complex interplay between emergent degrees of freedom leading to interesting physical phenomena in this $3d$-$4f$-based double perovskite that may provide deep insights that are relevant in the context of novel materials with competing magnetic order.

ACKNOWLEDGMENTS

S.K. acknowledges support from IIT Madras. P.K. acknowledges funding by the Science and Engineering Research Board and the Department of Science and Technology, India, through research grants. B.R.K.N. would like to acknowledge the funding from Department of Science and Technology, India, through Grant No. CRG/2020/004330.

[1] L. Balents, Nature (London) **464**, 199 (2010).
[2] H. Y. Hwang, Y. Iwasa, M. Kawasaki, B. Keimer, N. Nagaosa, and Y. Tokura, Nat. Mater. **11**, 103 (2012).
[3] P. Khuntia, J. Magn. Magn. Mater. **489**, 165435 (2019).
[4] P. Khuntia, M. Velazquez, Q. Barthélemy, F. Bert, E. Kermarrec, A. Legros, B. Bernu, L. Messio, A. Zorko, and P. Mendels, Nat. Phys. **16**, 469 (2020).
[5] B. Koteswararao, P. Khuntia, R. Kumar, A. V. Mahajan, A. Yogi, M. Baenitz, Y. Skourski, and F. C. Chou, Phys. Rev. B **95**, 180407(R) (2017).
[6] P. Khuntia, R. Kumar, A. V. Mahajan, M. Baenitz, and Y. Furukawa, Phys. Rev. B **93**, 140408(R) (2016).
[7] L. M. Fisher, A. V. Kalinov, I. F. Voloshin, N. A. Babushkina, D. I. Khomskii, Y. Zhang, and T. T. M. Palstra, Phys. Rev. B **70**, 212411 (2004).
[8] N. V. Baranov, A. V. Proshkin, C. Czternasty, M. Meißner, A. Podlesnyak, and S. M. Podgornykh, Phys. Rev. B **79**, 184420 (2009).
[9] A. K. Pathak, D. Paudyal, W. T. Jayasekara, S. Calder, A. Kreyssig, A. I. Goldman, K. A. Gschneidner, and V. K. Pecharsky, Phys. Rev. B **89**, 224411 (2014).
[10] B. S. Shivaram, B. Dorsey, D. G. Hinks, and P. Kumar, Phys. Rev. B **89**, 161108(R) (2014).
[11] M. E. Gruner, W. Keune, B. Roldan Cuenya, C. Weis, J. Landers, S. I. Makarov, D. Klar, M. Y. Hu, E. E. Alp, J. Zhao, M. Krautz, O. Gutfleisch, and H. Wende, Phys. Rev. Lett. **114**, 057202 (2015).
[12] L. V. B. Diop and O. Isnard, Phys. Rev. B **97**, 014436 (2018).

[13] T. Arh, B. Sana, M. Pregelj, P. Khuntia, Z. Jagličić, M. D. Le, P. K. Biswas, P. Manuel, L. Mangin-Thro, A. Ozarowski, and A. Zorko, Nat. Mater. **21**, 416 (2022).

[14] S. Kundu, A. Hossain, P. K. S., R. Das, M. Baenitz, P. J. Baker, J.-C. Orain, D. C. Joshi, R. Mathieu, P. Mahadevan, S. Pujari, S. Bhattacharjee, A. V. Mahajan, and D. D. Sarma, Phys. Rev. Lett. **125**, 117206 (2020).

[15] J. Khatua, M. Gomilšek, J. C. Orain, A. M. Strydom, Z. Jagličić, C. V. Colin, S. Petit, A. Ozarowski, L. Mangin-Thro, K. Sethupathi, M. S. R. Rao, A. Zorko, and P. Khuntia, Commun. Phys. **5**, 99 (2022).

[16] R. Kumar, P. Khuntia, D. Sheptyakov, P. G. Freeman, H. M. Rønnow, B. Koteswararao, M. Baenitz, M. Jeong, and A. V. Mahajan, Phys. Rev. B **92**, 180411(R) (2015).

[17] P. Khuntia, M. Mariani, M. C. Mozzati, L. Sorace, F. Orsini, A. Lascialfari, F. Borsa, C. Maxim, and M. Andruh, Phys. Rev. B **80**, 094413 (2009).

[18] P. Khuntia, A. Strydom, F. Steglich, and M. Baenitz, Phys. Status Solidi B **250**, 525 (2013).

[19] M. Brando, A. Kerkau, A. Todorova, Y. Yamada, P. Khuntia, T. Förster, U. Burkhard, M. Baenitz, and G. Kreiner, J. Phys. Soc. Jpn. **85**, 084707 (2016).

[20] R. Sarkar, R. Nath, P. Khuntia, H. S. Jeevan, P. Gegenwart, and M. Baenitz, J. Phys.: Condens. Matter **24**, 045702 (2012).

[21] A. Bhalla, R. Guo, and R. Roy, Mater. Res. Innovations **4**, 3 (2000).

[22] J. Blasco, J. García, G. Subías, J. Stankiewicz, J. A. Rodríguez-Velamazán, C. Ritter, J. L. García-Muñoz, and F. Fauth, Phys. Rev. B **93**, 214401 (2016).

[23] A. N. Vasiliev, O. S. Volkova, L. S. Lobanovskii, I. O. Troyanchuk, Z. Hu, L. H. Tjeng, D. I. Khomskii, H.-J. Lin, C. T. Chen, N. Tristan, F. Kretzschmar, R. Klingeler, and B. Büchner, Phys. Rev. B **77**, 104442 (2008).

[24] S.-W. Cheong and M. Mostovoy, Nat. Mater. **6**, 13 (2007).

[25] R. J. Cava, B. Batlogg, J. J. Krajewski, R. Farrow, L. W. Rupp, A. E. White, K. Short, W. F. Peck, and T. Kometani, Nature (London) **332**, 814 (1988).

[26] K.-I. Kobayashi, T. Kimura, H. Sawada, K. Terakura, and Y. Tokura, Nature (London) **395**, 677 (1998).

[27] A. M. Cook and A. Paramekanti, Phys. Rev. Lett. **113**, 077203 (2014).

[28] A. M. Cook, S. Matern, C. Hickey, A. A. Aczel, and A. Paramekanti, Phys. Rev. B **92**, 020417(R) (2015).

[29] T. Dey, A. V. Mahajan, R. Kumar, B. Koteswararao, F. C. Chou, A. A. Omrani, and H. M. Ronnow, Phys. Rev. B **88**, 134425 (2013).

[30] B. Singh, M. Vogl, S. Wurmehl, S. Aswartham, B. Büchner, and P. Kumar, Phys. Rev. Res. **2**, 013040 (2020).

[31] J. Khatua, T. Arh, S. B. Mishra, H. Luetkens, A. Zorko, B. Sana, M. S. R. Rao, B. R. K. Nanda, and P. Khuntia, Sci. Rep. **11**, 6959 (2021).

[32] C. R. Wiebe, J. E. Greedan, P. P. Kyriakou, G. M. Luke, J. S. Gardner, A. Fukaya, I. M. Gat-Malureanu, P. L. Russo, A. T. Savici, and Y. J. Uemura, Phys. Rev. B **68**, 134410 (2003).

[33] S. Vasala and M. Karppinen, Prog. Solid State Chem. **43**, 1 (2015).

[34] N. Hur, I. K. Jeong, M. F. Hundley, S. B. Kim, and S.-W. Cheong, Phys. Rev. B **79**, 134120 (2009).

[35] J. Y. Moon, M. K. Kim, D. G. Oh, J. H. Kim, H. J. Shin, Y. J. Choi, and N. Lee, Phys. Rev. B **98**, 174424 (2018).

[36] K. D. Truong, M. P. Singh, S. Jandl, and P. Fournier, J. Phys.: Condens. Matter **23**, 052202 (2011).

[37] S. Kumar, G. Giovannetti, J. van den Brink, and S. Picozzi, Phys. Rev. B **82**, 134429 (2010).

[38] D. Choudhury, P. Mandal, R. Mathieu, A. Hazarika, S. Rajan, A. Sundaresan, U. V. Waghmare, R. Knut, O. Karis, P. Nordblad, and D. D. Sarma, Phys. Rev. Lett. **108**, 127201 (2012).

[39] R. I. Dass and J. B. Goodenough, Phys. Rev. B **67**, 014401 (2003).

[40] R. Booth, R. Fillman, H. Whitaker, A. Nag, R. Tiwari, K. Ramanujachary, J. Gopalakrishnan, and S. Lofland, Mater. Res. Bull. **44**, 1559 (2009).

[41] J. B. Goodenough, Phys. Rev. **100**, 564 (1955).

[42] A. Banerjee, J. Sannigrahi, S. Giri, and S. Majumdar, Phys. Rev. B **98**, 104414 (2018).

[43] H. Y. Choi, J. Y. Moon, J. H. Kim, Y. J. Choi, and N. Lee, Crystals **7**, 67 (2017).

[44] S. M. Wang, S. H. Zheng, L. Lin, Y. S. Tang, J. H. Zhang, R. Chen, J. F. Wang, C. L. Lu, Z. B. Yan, X. P. Jiang, and J.-M. Liu, J. Appl. Phys. **126**, 084102 (2019).

[45] G. Sharma, J. Saha, S. Kaushik, V. Siruguri, and S. Patnaik, Appl. Phys. Lett. **103**, 012903 (2013).

[46] H. S. Nair, R. Pradheesh, Y. Xiao, D. Cherian, S. Elizabeth, T. Hansen, T. Chatterji, and T. Brückel, J. Appl. Phys. **116**, 123907 (2014).

[47] R. P. Madhogaria, R. Das, E. M. Clements, V. Kalappattil, M. H. Phan, H. Srikanth, N. T. Dang, D. P. Kozlenko, and N. S. Bingham, Phys. Rev. B **99**, 104436 (2019).

[48] H. M. Rietveld, J. Appl. Crystallogr. **2**, 65 (1969).

[49] J. Rodríguez-Carvajal, Phys. B (Amsterdam) **192**, 55 (1993).

[50] J. Blasco, J. L. García-Muñoz, J. García, G. Subías, J. Stankiewicz, J. A. Rodríguez-Velamazán, and C. Ritter, Phys. Rev. B **96**, 024409 (2017).

[51] D. Mazumdar and I. Das, J. Appl. Phys. **129**, 063901 (2021).

[52] A. Pal, S. Ghosh, A. G. Joshi, S. Kumar, S. Patil, P. K. Gupta, P. Singh, V. Gangwar, P. Prakash, R. K. Singh, E. F. Schwier, M. Sawada, K. Shimada, A. Ghosh, A. Das, and S. Chatterjee, J. Phys.: Condens. Matter **31**, 275802 (2019).

[53] A. Pal, P. Singh, V. K. Gangwar, A. G. Joshi, P. Khuntia, G. D. Dwivedi, P. K. Gupta, M. Alam, K. Anand, K. Sethupathi, A. K. Ghosh, and S. Chatterjee, J. Phys.: Condens. Matter **32**, 215801 (2020).

[54] NIST X-ray Photoelectron Spectroscopy Database, version 3.5, National Institute of Standards and Technology, Gaithersburg, MD.

[55] S. Laureti, E. Agostinelli, G. Scavia, G. Varvaro, V. R. Albertini, A. Generosi, B. Paci, A. Mezzi, and S. Kaciulis, Appl. Surf. Sci. **254**, 5111 (2008).

[56] C. A. F. Vaz, D. Prabhakaran, E. I. Altman, and V. E. Henrich, Phys. Rev. B **80**, 155457 (2009).

[57] R. R. Das, P. N. Lekshmi, S. Das, and P. Santhosh, J. Alloys Compd. **773**, 770 (2019).

[58] K. Binder and A. P. Young, Rev. Mod. Phys. **58**, 801 (1986).

[59] R. Kumar, T. Dey, P. M. Ette, K. Ramesha, A. Chakraborty, I. Dasgupta, R. Eremina, S. Tóth, A. Shahee, S. Kundu, M. Prinz-Zwick, A. A. Gippius, H. A. K. von Nidda, N. Büttgen,

P. Gegenwart, and A. V. Mahajan, Phys. Rev. B **99**, 144429 (2019).
[60] C. Djurberg, P. Svedlindh, P. Nordblad, M. F. Hansen, F. Bødker, and S. Mørup, Phys. Rev. Lett. **79**, 5154 (1997).
[61] M. D. Mukadam, S. M. Yusuf, P. Sharma, S. K. Kulshreshtha, and G. K. Dey, Phys. Rev. B **72**, 174408 (2005).
[62] A. Arrott, Phys. Rev. **108**, 1394 (1957).
[63] I. Yeung, R. M. Roshko, and G. Williams, Phys. Rev. B **34**, 3456 (1986).
[64] G. Herzer, M. Fähnle, T. Egami, and H. Kronmüller, Phys. Status Solidi B **101**, 713 (1980).
[65] K. A. Gschneidner Jr, V. K. Pecharsky, and A. O. Tsokol, Rep. Prog. Phys. **68**, 1479 (2005).
[66] V. Provenzano, A. J. Shapiro, and R. D. Shull, Nature (London) **429**, 853 (2004).
[67] O. Tegus, E. Brück, K. H. J. Buschow, and F. R. de Boer, Nature (London) **415**, 150 (2002).
[68] M. E. Zhitomirsky, Phys. Rev. B **67**, 104421 (2003).
[69] M.-H. Phan and S.-C. Yu, J. Magn. Magn. Mater. **308**, 325 (2007).
[70] P. Lampen, N. S. Bingham, M. H. Phan, H. Srikanth, H. T. Yi, and S. W. Cheong, Phys. Rev. B **89**, 144414 (2014).
[71] H. Oesterreicher and F. T. Parker, J. Appl. Phys. **55**, 4334 (1984).
[72] C. Li, L. Wang, X. Li, C. Zhu, R. Zhang, H. Wang, and S. Yuan, Mater. Chem. Phys. **202**, 76 (2017).
[73] V. Singh, P. Bag, R. Rawat, and R. Nath, Sci. Rep. **10**, 6981 (2020).
[74] E. Granado, A. García, J. A. Sanjurjo, C. Rettori, I. Torriani, F. Prado, R. D. Sánchez, A. Caneiro, and S. B. Oseroff, Phys. Rev. B **60**, 11879 (1999).
[75] J. Laverdière, S. Jandl, A. A. Mukhin, V. Y. Ivanov, V. G. Ivanov, and M. N. Iliev, Phys. Rev. B **73**, 214301 (2006).
[76] M. N. Iliev, M. V. Abrashev, A. P. Litvinchuk, V. G. Hadjiev, H. Guo, and A. Gupta, Phys. Rev. B **75**, 104118 (2007).
[77] M. Balkanski, R. F. Wallis, and E. Haro, Phys. Rev. B **28**, 1928 (1983).
[78] M. N. Iliev, P. Padhan, and A. Gupta, Phys. Rev. B **77**, 172303 (2008).
[79] G. Kresse and D. Joubert, Phys. Rev. B **59**, 1758 (1999).
[80] G. Kresse and J. Furthmüller, Phys. Rev. B **54**, 11169 (1996).
[81] S. L. Dudarev, G. A. Botton, S. Y. Savrasov, C. J. Humphreys, and A. P. Sutton, Phys. Rev. B **57**, 1505 (1998).
[82] P. Parida, R. Kashikar, A. Jena, and B. Nanda, J. Phys. Chem. Solids **123**, 133 (2018).